Supporting Information for "Characteristic Slow-Slip Events on the Superstition Hills Fault, Southern California"

Ellis J. Vavra[1], Yuri Fialko[1], Thomas Rockwell[2], Roger Bilham[3], Petra Štěpančíková[4], Jakub Stemberk[4], Petr Tábořík[4], Josef Stemberk[4]

[1]Institute of Geophysics and Planetary Physics, Scripps Institution of Oceanography, University of California, San Diego, La Jolla, CA, USA

[2]Department of Geological Sciences, San Diego State University, San Diego, CA, USA

[3]Cooperative Institute for Research in Environmental Sciences, University of Colorado, Boulder, Boulder, CO, USA

[4]Institute of Rock Structure and Mechanics, Czech Academy of Sciences, Prague, Czech Republic

Contents

Introduction

This document contains supplementary text and figures referenced in the main text.

Text S1: Description of the Creepmeters

The Colorado (COL) creepmeter consists of a 6-m-long, 4-mm-diameter pultruded carbon rod anchored to the east side of the fault, which crosses the fault at 30° within a 2 cm internal diameter plastic conduit (Bilham & Castillo, 2020). The instrument is thereby anchored ±1.5m from the fault trace. Its free end on the west side of the fault is held in tension by a 0.15-mm-diameter, 19-strand, nylon-coated, stainless-steel wire spooled on a 1 N constant-tension spring motor. The wire is wrapped once around the shaft of a low friction rotary Hall sensor causing the shaft to rotate in response to fault slip. Each complete rotation of the shaft results in a 4.5 V linear voltage change (corresponding to ∼11.5 mm of dextral fault slip) that resets to zero at a 360°-0 transition, thereby permitting an extended measurement range of 1.3 m limited by the length of the

Corresponding author: Ellis J. Vavra, evavra@ucsd.edu

spooled wire. The output is measured once per minute to a precision of 3 µm. The 39 mm extended creep event resulted in more than two complete shaft rotations that have been removed in Figure 2. In the 13 years prior to the 2023 slip event the creepmeter had recorded a linear featureless fault slip rate of 0.3 mm/year.

The TM-71 opto-mechanical creepmeter measures dip-slip, strike-slip, dilation, and rotation between two blocks separated by a discontinuity at daily intervals (Košťák, 1969; Klimeš et al., 2012; Martí et al., 2013). Total vector of fault displacement u is then calculated based on these components:

$$u = \sqrt{{u_{strike-slip}}^2 + {u_{dip-slip}}^2 + {u_{dilation}}^2} \tag{1}$$

The instrument uses optical interference that appears when spirals on two glass sheets slide over one another, and characteristic Moiré interference occur (Kostak & Popp, 1966; Martí et al., 2013). The interference effect can be transformed into a metric system through the number of strips and axis of symmetry (Kostak & Popp, 1966). The value of displacement between the centres of glass sheets is determined by the number of interference strips, and the direction of displacement is shown by the main axis of symmetry of the optical effect. All possible relative movements of the blocks are measured once per day to a precision of 1 μm. The relative rotation between two blocks are measured to a precision of $> 3.2 \times 10^4$ rad ($\approx 0.018°$).

Text S3: InSAR offset estimation procedure

Surface offsets along the trace of the SHF are the primary dataset documenting past coseismic and aseismic fault ruptures (e.g., Allen et al., 1972; Sharp et al., 1986; Rymer et al., 2002; Wei et al., 2011). We estimate surface offsets for the 2023 SSE by averaging InSAR pixels on opposite sides of the mapped fault trace at regular intervals. We select fault-perpendicular 10 km-by-250 m swaths at 250 m intervals along the fault and difference the means of bins of pixels on either side of the fault to estimate offsets. Some large outlier pixels exist, in particular near the highly localized slip patch near Imler Road (Figures 3 & 4), due to decorrelation and/or unwrapping errors. To identify outliers, we utilize the z-score,

$$Z_i = \frac{x_i - \mu}{\sigma} \tag{2}$$

which describes deviation of a value x_i from the mean μ with respect to the standard deviation σ. We modify Equation 1 in order to emphasize the detection of outlier data points by computing the mean $\hat{\mu}$ and standard deviation $\hat{\sigma}$ of the data x_j for $j \neq i$, resulting in the adjusted z-score $\hat{Z}_i = \frac{x_i - \hat{\mu}}{\hat{\sigma}}$ which is exaggerated compared to Z_i due to the relative changes in the mean $\hat{\mu}$ and standard deviation $\hat{\sigma}$.

Initially, we bin data within ±200 m of the fault and compute $\hat{Z}_i$ for all pixels in each bin. We then fit a straight line to each group of pixels with $\hat{Z}_i \leq 1$ to determine if slip is localized or distributed. If the signs of the slopes are the same, slip is determined to be distributed across the fault trace; if the signs are opposite, then slip is discontinuous. Since we are only interested in removing extreme outliers associated with high amplitude, localized slip, we compute fault offsets simply using all pixels within ±100 m bins if distributed slip is identified. If slip is localized, we omit pixels with $\hat{Z}_i > 1$ and use the means and standard deviations of the remaining pixels to estimate fault offsets and their uncertainties. This procedure produces near-field (i.e. "on-fault") surface offset estimates which are suitable for comparison with field and creepmeter measurements of observed fault slip (although there still lie differences in measurement aperture which bias each observation). However, examination of individual profiles (Figure S4) shows that along much of the northern portion of the fault, where deformation is distributed, maximum deformation occurs off-fault.

To quantify the "maximum offsets" at the surface for distributed deformation, we identify the shear zone width using the gradients of the displacements and compute offsets at the edges of the shear zone. We smooth the profiles using a Savitsky-Golay filter (window of 35 and polynomial order of 3), interpolate the smoothed profiles to 10 m resolution, and then compute the displacement gradient du/dx of the smoothed and interpolated profiles. We estimate the width of the distributed shear zone by finding the nearest-fault location where $du/dx = 0$ on either side of the fault. We place a maximum shear zone width of 2000 m, determined by manual inspection of the profiles, in order to avoid erroneous estimates due to residual atmospheric noise. To estimate the maximum off-fault displacements, we use the mean of original InSAR pixels within ±100 m of the identified shear zone edges. We also estimate uncertainties by computing the standard deviations within the same bins. Results for both the on-fault and off-fault displacements are shown in Figure 4B.

Text S4: Finite Fault Inversion Procedure

We use the Sentinel-1A InSAR measurements of slip during the 2023 SSE to invert for the 3D distribution of slip along the SHF. We mapped a simplified version of the active SHF through combination of its representation in the USGS Quaternary fault database (USGS, 2020) and the observed surface displacements due to 2023 slip (Figure 3). We generate a triangular mesh by assuming a vertical fault geometry and tessellating triangular elements 10 km depth. The minimum element dimensions are 0.25-0.3 km t the surface and increase geometrically with depth. The resulting mesh has 492 elements. From the fault mesh geometry, we compute fault Greens functions for surface displacements using a Python implementation for triangular dislocation elements (Nikkhoo & Walter, 2015) from Ben Thompson (`https://github.com/tbenthompson/cutde`).

Since the fault geometry (and thus Greens functions) is fixed, the resulting inverse problem is linear and over-determined. We solve for the optimal slip distribution along the fault using least squares. We generate Greens functions for dextral fault slip and project them to the satellite line-of-sight (LOS). We add a slip-smoothness constraint that uses first-differences between neighboring TDEs to limit sharp changes in the slip distribution (e.g., Aster et al., 2018). We also include a soft zero-slip boundary condition to enforce the assumption that slip tapers to zero at the edges of the rupture. The resulting set of linear equations is

$$\begin{bmatrix} \boldsymbol{G} \\ \mu \boldsymbol{R} \\ \eta \boldsymbol{L} \end{bmatrix} \begin{bmatrix} \boldsymbol{m} \end{bmatrix} = \begin{bmatrix} \boldsymbol{d} \\ \boldsymbol{0} \\ \boldsymbol{0} \end{bmatrix} \tag{3}$$

where $\boldsymbol{G}$ are the LOS-projected Greens functions, $\boldsymbol{R}$ is the first-difference smoothness operator, $\boldsymbol{L}$ is the zero-slip boundary operator (applied to TDEs at the bottom and lateral edges of the fault, with the exception of corner elements at the surface), μ and η are weights applied to the smoothness and zero-slip regularization terms, respectively, $\boldsymbol{d}$ is composed of InSAR LOS measurements, and $\boldsymbol{m}$ is the modelled slip distribution. We solve Equation 2 for $\boldsymbol{m}$ using least-squares with a positivity constraint to enforce dextral-only slip.

To determine values for the regularization weights μ and η that appropriately balance model complexity (i.e. slip heterogeneity) and smoothness, we perform a grid search

over $10^{-3} - 10^{3}$ for both parameters (Figure S5). We use 20 samples for each parameter, resulting in 400 models. We find large increases in the root-mean-square (RMS) of model residuals for $\mu > 5 \times 10^{1}$ (Figure S5). Visual inspection of associated models shows systematic residuals with fault-like patterns, suggesting $\mu > 5 \times 10^{1}$ generates unrealistically smooth slip distributions. For models with $\mu < 5 \times 10^{1}$, there is little change in RMS with increased η. This suggests that little slip near the edges of the model domain is required to fit the data, which is consistent with slip being limited to the extent of shallow sediments (Kohler & Fuis, 1986). Our preferred model (blue dot in Figure S5) uses $\mu = 0.7$ and $\eta = 1.4$ (Figure 5)

To improve the computational efficiency of our inversions without reducing the quantitative information in our dataset, we down-sample the full InSAR displacement field using a quad-tree algorithm (Jonsson, 2002; Simons, 2002). Thus, in all inversions, $\boldsymbol{d}$ is composed of down-sampled data rather than the full-resolution InSAR pixels. We allow the size of the quad-tree cells to approach full resolution ($\sim$ 100 m) where gradients are high (i.e. near the fault trace) and place a maximum size of 2 km where gradients are low (Figure S6).

To avoid oversampling regions of high-frequency noise or residual troposphere noise, we use an iterative model-based approach (Wang & Fialko, 2018). First, we generate an initial displacement field using a prescribed synthetic slip distribution. We then apply the quad-tree algorithm to the initial displacement field model in order to obtain a first-order approximation of the appropriate sampling distribution, with dense sampling near the fault trace and more sparse sampling in the far-field. For the grid search, we only use the initial sampling distribution in order to accurately compare model performance across the ranges of regularization parameters μ and η. After determining reasonable values for μ and η, we apply the quad-tree sampling obtained from the starting model to the real data (Figures 3 & S6) and repeat the process several times, each time re-sampling based on the previous model prediction. To obtain our final preferred model, we use three iterations; Figure S6 shows the final down-sampled dataset.

Text S5: Possible Triggering of the 2023 SSE

While most documented SHF slip events are triggered by regional earthquakes, there is no clear connection to seismicity for the 2023 or 2006 SSEs (Wei et al., 2009). We investigated both regional and global seismicity to confirm whether the 2023 event was spon-

taneous or dynamically triggered. Over 29-30 April 2023, four M_w 4+ earthquakes occurred in the Salton Trough and within 40 km of the nucleation site of the 2023 SSE (Figure S7). The first event occurred at the Heber geothermal field and a sequence of three $M_w \approx 4.3$ events followed at the Salton Sea geothermal field approximately 18 hours after the Heber event. We inspected a Sentinel-1 interferogram spanning 22 April 2023 - 3 May 2023 and found no discernible deformation along the SHF which may have been instantaneously triggered by dynamic stresses associated with any of the late-April 2023 Salton Trough events. While perturbations to the pore pressure state of the SHF due to these events (e.g., Brodsky, 2003) may have contributed to the subsequent occurrence of the 2023 SSE, we find no evidence for fault slip prior to 3 May 2023.

Several additional regional and global earthquakes occurred during the 3-15 May 2023 Sentinel-1 interferogram epoch. An aftershock of the M_w 4.1 Heber event occurred on 6 May, which was the largest event in the Salton Trough between 3-15 May (Figure S7). In addition, a M_w 6.4 event in Japan on 4 May, a M_w 7.6 event near Samoa on 10 May, and a M_w 5.2 near Lassen, CA on 12 May occurred within the timeframe of the interferogram. We suggest dynamic triggering is unlikely to have initiated the 2023 event as slip during previous triggered events on the SHF only occurred during and immediately after the passing seismic waves, resulting in a step-like signal (Wei et al., 2011). In addition, the relatively stronger ground shaking less than two weeks prior due to the local M_w 4+ events did not initiate slip on the SHF. While prolonged SSEs have been shown to occur on the Southern San Andreas Fault in response to teleseismic surface waves (Tymofyeyeva et al., 2019), the similarity in the temporal history of the 2023 SSE with the 2006 SSE, and lack thereof with respect to observed dynamically triggered SHF events leads us to suggest that the 2023 event was most likely spontaneous.

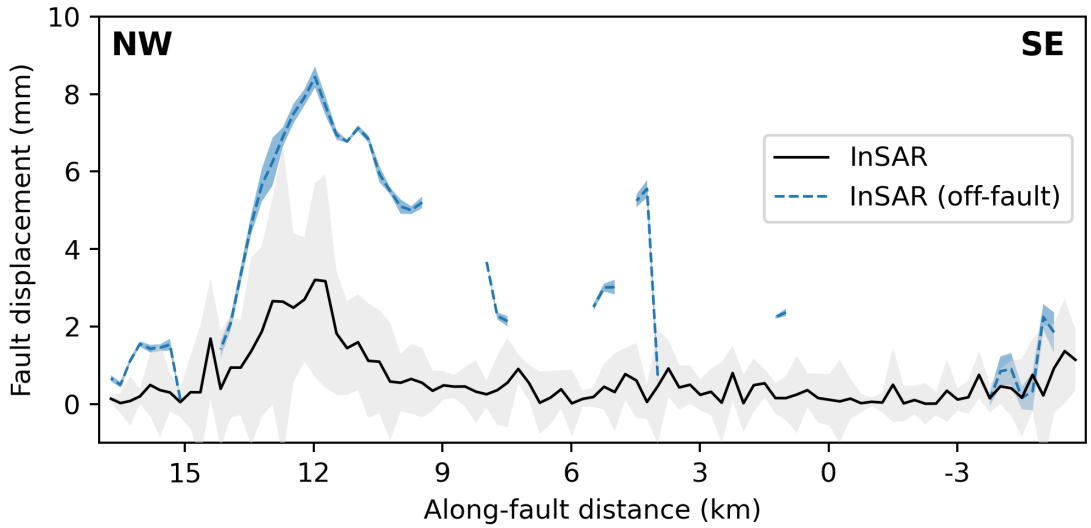

Figure S1. Surface offsets calculated from a Sentinel-1 interferogram spanning 3-15 May 2023. Maximum slip of ∼5-8 mm is observed at about ∼14 km to ∼10 km along the fault. Along-strike distances are referenced to the location of the creepmeters. Detected slip outside of ∼15 km to ∼8 km is likely due to residual atmospheric noise (see Figures 2B and S4).

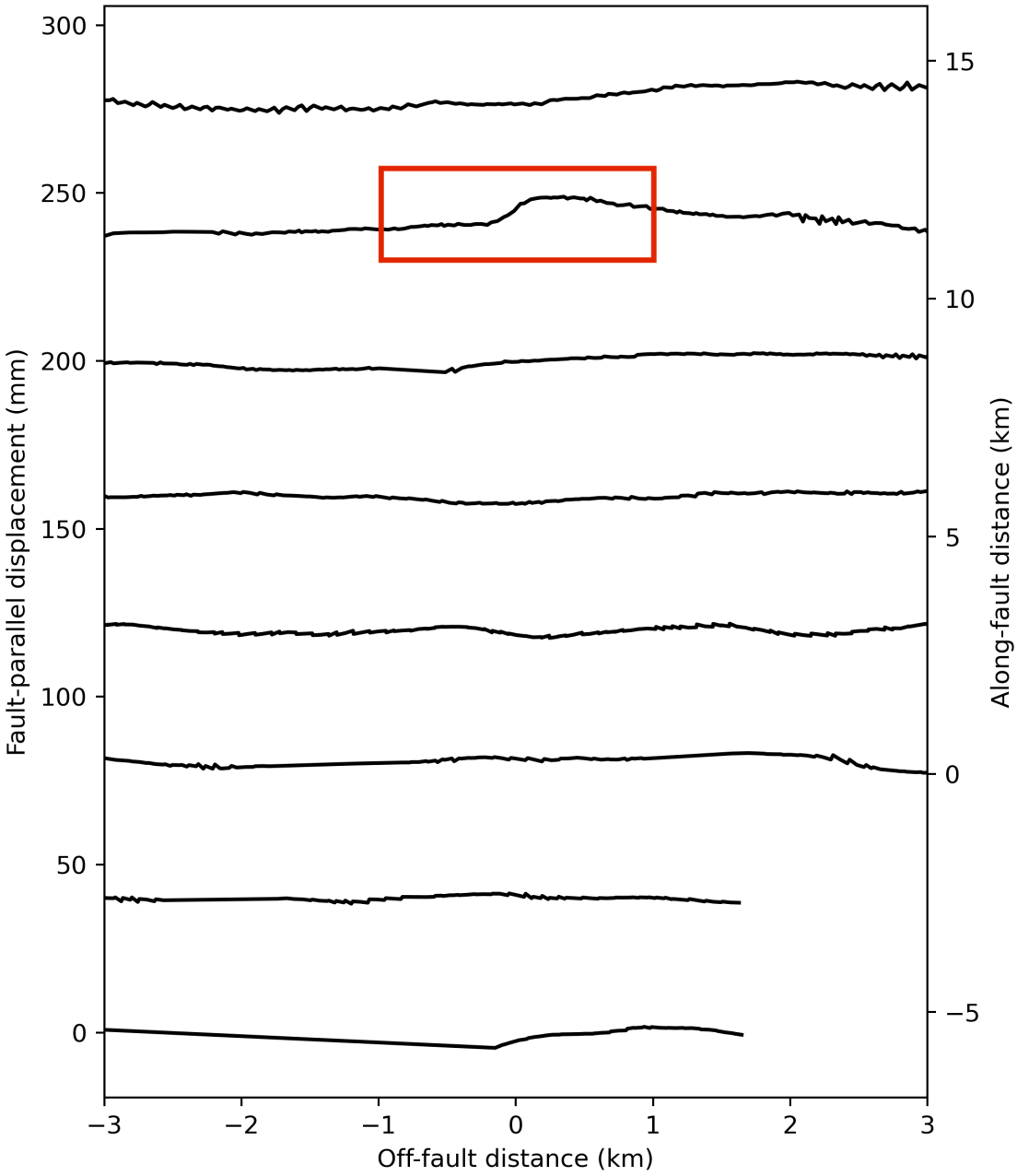

Figure S2. Example displacement profiles at 3 km intervals for an interferogram spanning 3-15 May 2023. The red box indicates distributed surface deformation due to fault slip ~11 km north of the creepmeters. To improve visualization, this figure uses 10 km-by-100 m profiles at 3 km intervals instead of the profiles used in computing fault offsets (see Text S3).

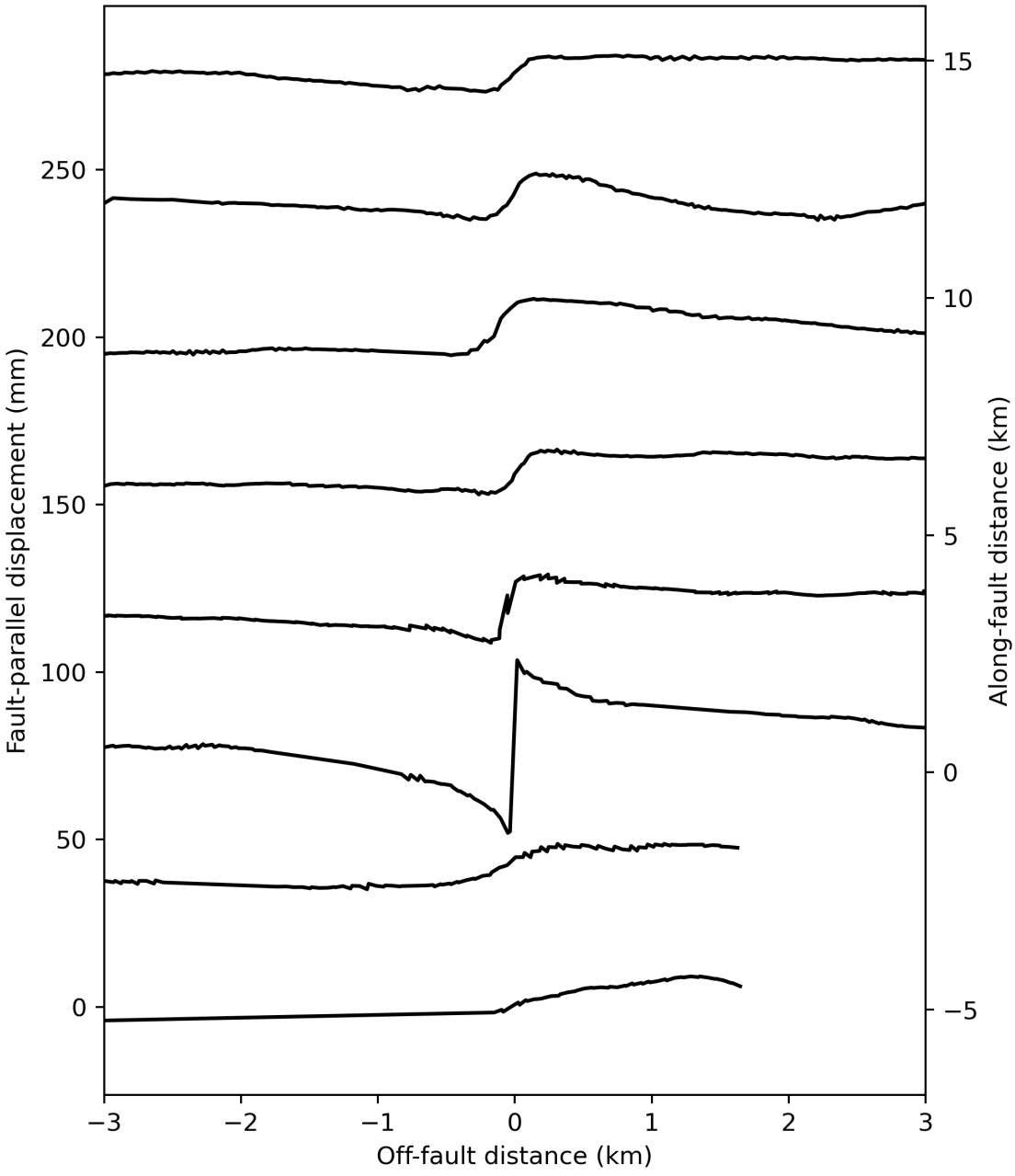

Figure S3. Same as Figure S3 but for 3 May 2023 to 8 June 2023 (same timeframe as Figure 4). Variations in slip localization at the surface is apparent, with highly localized deformation only occurring within several km of the creepmeters ($y \approx -2 - 3$ km; Figure 4).

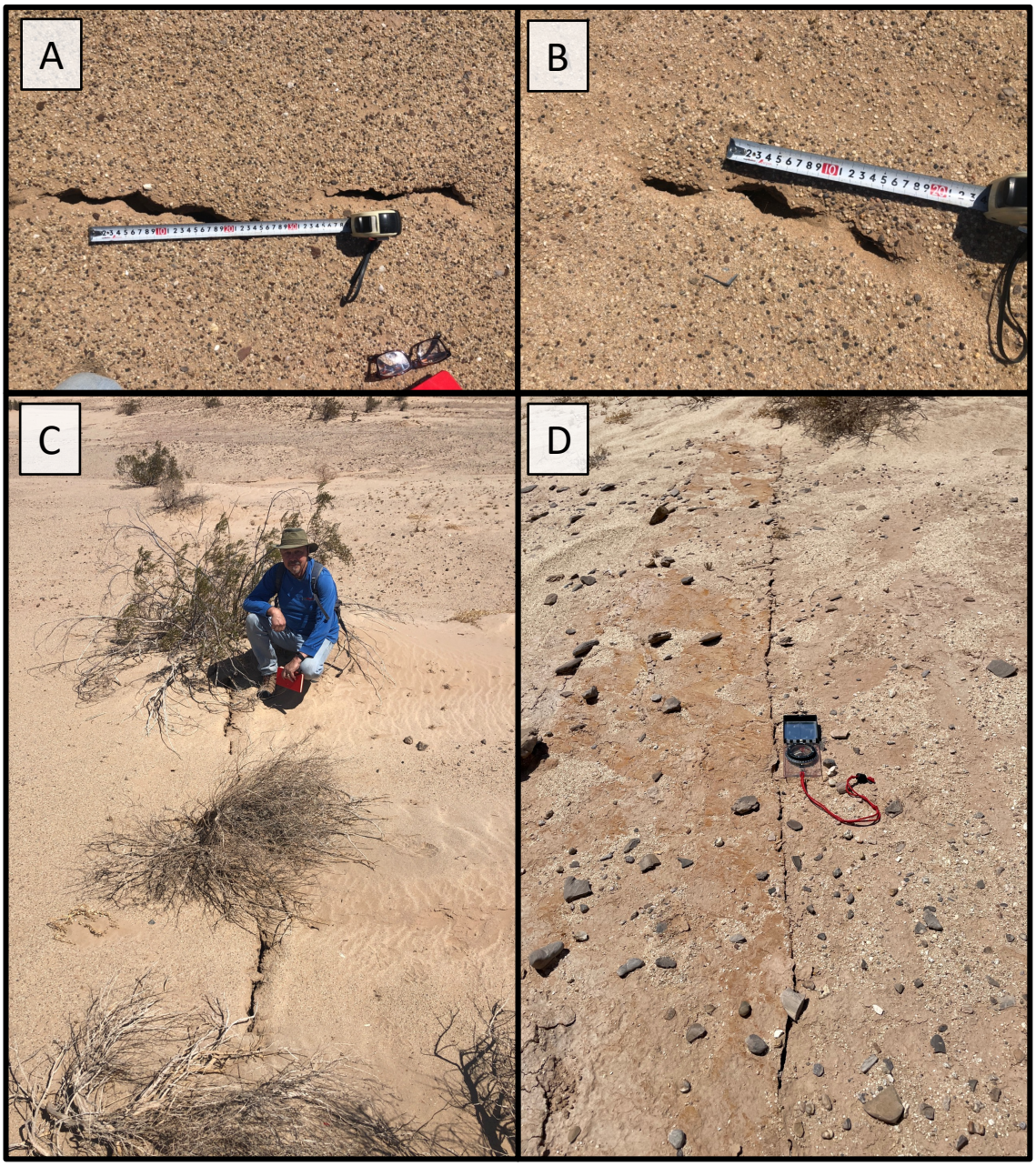

Figure S4. Additional photos of the 2023 surface rupture from the 11 June 2023 field survey.

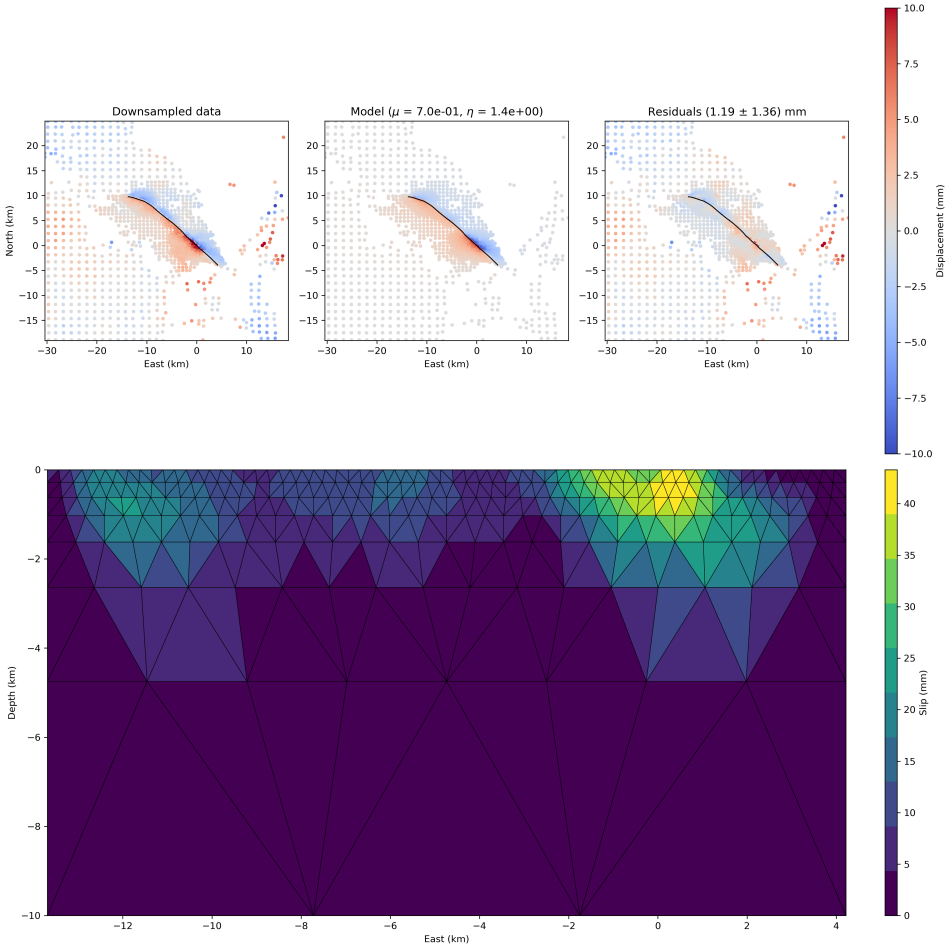

Figure S5. Quad-tree down-sampling and slip distribution associated with the preferred finite fault model. The top row shows InSAR data, model prediction, and resiuals for the the final iteration of quad-tree down-sampling (see Text S4). The bottom panel shows a 2D view of the inverted slip distribution (same model as Figure 5).

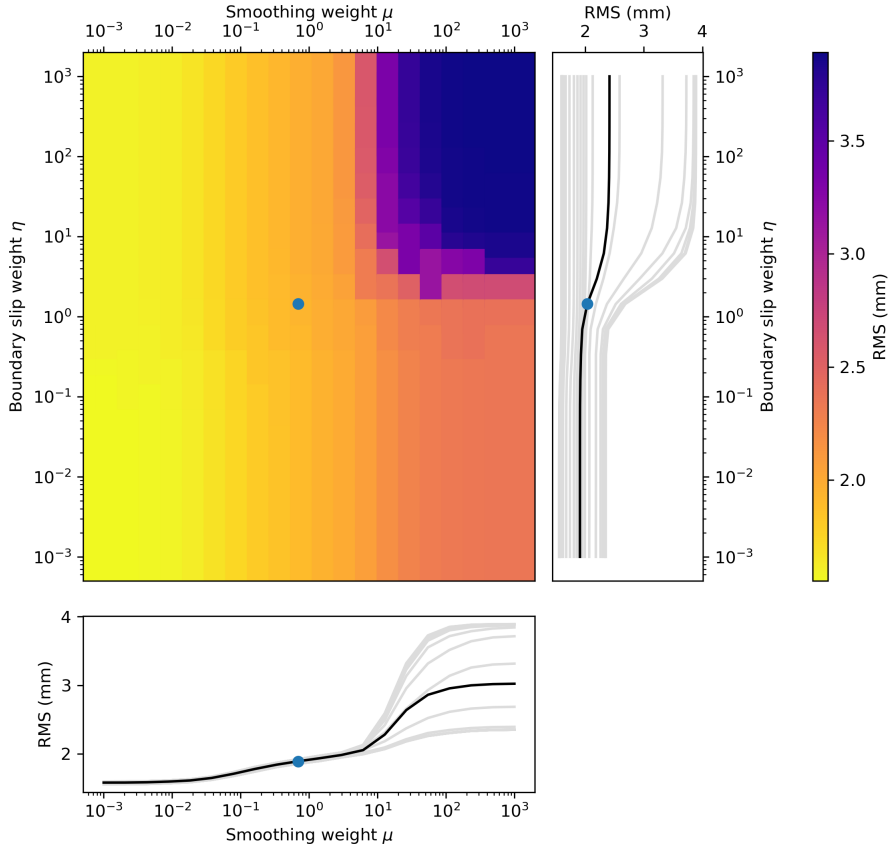

Figure S6. Grid search results over values of smoothness μ and edge slip η constraints. Values between 10^{-3} – 10^{3} were tested for each parameter, with 20 samples each. The main panel is color-coded by the root-mean-square (RMS) of model residuals. The bottom panel shows the RMS values with respect to μ for with each value of η (gray lines); the RMS values averaged across all η are shown in black. The right panel is the same as the bottom, but for η. The blue dot in each panel indicates the preferred model with $\mu = 0.7$ and $\eta = 1.4$.

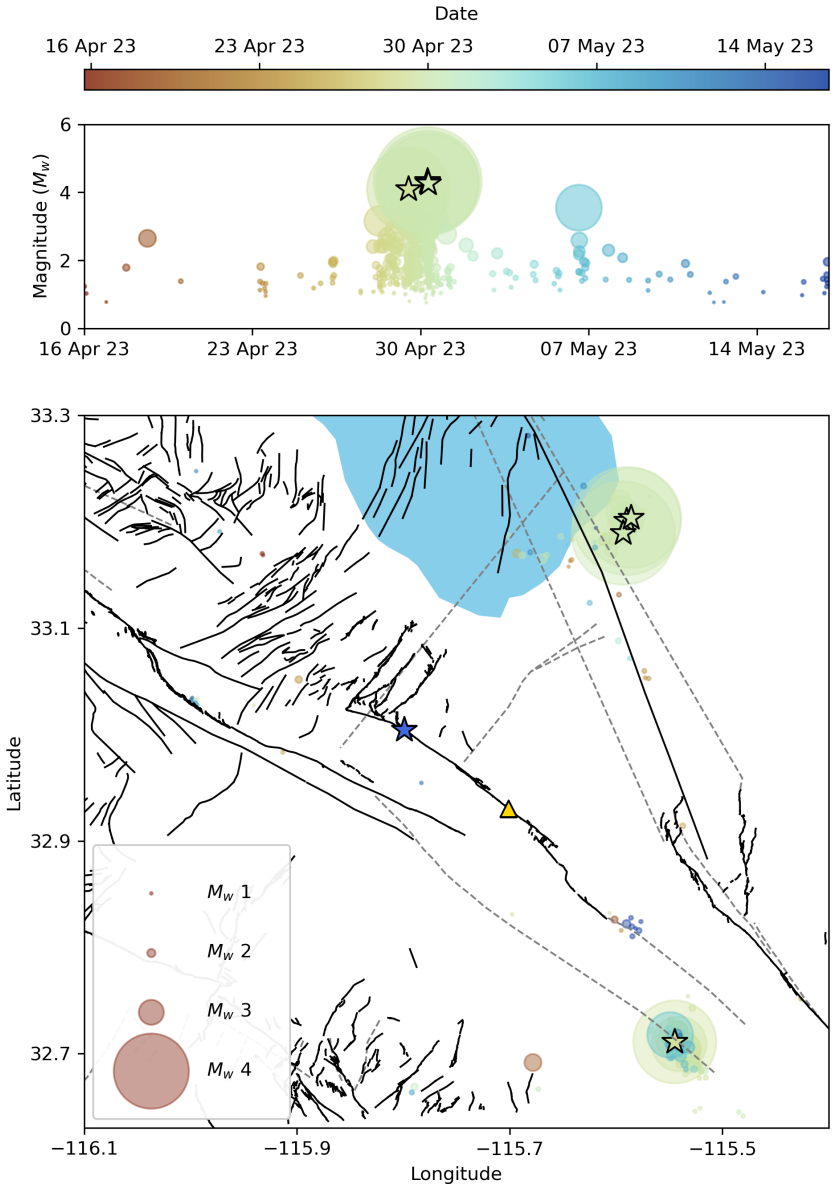

Figure S7. Local seismicity one month prior to slip being detected by the COL creepmeter (16 April 2023 - 16 May 2023). Quaternary faults are shown as black lines (USGS, 2020), while blind faults from the Southern California Earthquake Center Community Fault Model are shown as dashed gray lines (Shaw et al., 2015). The yellow triangle shows the location of creepmeters installed near Imler Road. The blue star indicates the nucleation site of initial slip on the SHF which initiated some time between 3-15 May 2023. The hypocenters of four M_w 4+ events occurring between 29-30 April 2023 are shown as light green stars.

References

Allen, C. R., Wyss, M., Brune, J. N., Grantz, A., & Wallace, R. E. (1972). *Displacements on the Imperial, Superstition Hills, and San Andreas Faults Triggered by teh Borrego Mountain Earthuake.* (Tech. Rep.).

Aster, R. C., Borchers, B., & Thurber, C. H. (2018). *Parameter estimation and inverse problems.* Elsevier.

Bilham, R., & Castillo, B. (2020). The July 2019 Ridgecrest, California, Earthquake Sequence Recorded by Creepmeters: Negligible Epicentral Afterslip and Prolonged Triggered Slip at Teleseismic Distances. *Seismological Research Letters*, *91*(2A), 707–720.

Brodsky, E. E. (2003). A mechanism for sustained groundwater pressure changes induced by distant earthquakes. *Journal of Geophysical Research*, *108*(B8), 2390.

Jonsson, S. (2002). Fault Slip Distribution of the 1999 Mw 7.1 Hector Mine, California, Earthquake, Estimated from Satellite Radar and GPS Measurements. *Bulletin of the Seismological Society of America*, *92*(4), 1377–1389.

Klimeš, J., Rowberry, M. D., Blahůt, J., Briestenský, M., Hartvich, F., Košťák, B., Rybář, J., Stemberk, J., & Štěpančíková, P. (2012). The monitoring of slow-moving landslides and assessment of stabilisation measures using an optical–mechanical crack gauge. *Landslides*, *9*(3), 407–415.

Kohler, W. M., & Fuis, G. S. (1986). Travel-time, time-term, and basement depth maps for the Imperial Valley region, California, from explosions. *Bulletin of the Seismological Society of America*, *76*(5), 1289–1303.

Kostak, B., & Popp, K. (1966). Moiré strain gauges. *Strain*, *2*(2), 5–16.

Košťák, B. (1969). A new device for in-situ movement detection and measurement. *Experimental Mechanics*, *9*(8), 374–379.

Martí, X., Rowberry, M. D., & Blahůt, J. (2013). A MATLAB® code for counting the moiré interference fringes recorded by the optical-mechanical crack gauge TM-71. *Computers & Geosciences*, *52*, 164–167.

Nikkhoo, M., & Walter, T. R. (2015). Triangular dislocation: an analytical, artefact-free solution. *Geophysical Journal International*, *201*(2), 1119–1141.

Rymer, M. J., Boatwright, J., Seekins, L. C., Yule, D., & Liu, J. (2002). Triggered Surface Slips in the Salton Trough Associated with the 1999 Hector Mine, Cal-

ifornia, Earthquake. *Bulletin of the Seismological Society of America*, *92*(4), 1300–1317.

Sharp, R. V., Rymer, M. J., & Lienkaemper, J. J. (1986). Surface displacement on the Imperial and Superstition Hills faults triggered by the Westmorland, California, earthquake of 26 April 1981. *Bulletin of the Seismological Society of America*, *76*(4), 949–965.

Shaw, J. H., Plesch, A., Tape, C., Suess, M. P., Jordan, T. H., Ely, G., Hauksson, E., Tromp, J., Tanimoto, T., Graves, R., Olsen, K., Nicholson, C., Maechling, P. J., Rivero, C., Lovely, P., Brankman, C. M., & Munster, J. (2015). Unified Structural Representation of the southern California crust and upper mantle. *Earth and Planetary Science Letters*, *415*, 1–15.

Simons, M. (2002). Coseismic Deformation from the 1999 Mw 7.1 Hector Mine, California, Earthquake as Inferred from InSAR and GPS Observations. *Bulletin of the Seismological Society of America*, *92*(4), 1390–1402.

Tymofyeyeva, E., Fialko, Y., Jiang, J., Xu, X., Sandwell, D., Bilham, R., Rockwell, T. K., Blanton, C., Burkett, F., Gontz, A., & Moafipoor, S. (2019). Slow Slip Event On the Southern San Andreas Fault Triggered by the 2017 Mw 8.2 Chiapas (Mexico) Earthquake. *Journal of Geophysical Research: Solid Earth*, *124*(9), 9956–9975.

USGS. (2020). *Quaternary Fault and Fold Database for the Nation.*

Wang, K., & Fialko, Y. (2018). Observations and modeling of co- and postseismic deformation due to the 2015 M_w 7.8 Gorkha (Nepal) earthquake. *J. Geophys. Res.*, *123*(1), 761–779.

Wei, M., Sandwell, D., & Fialko, Y. (2009). A silent M_w 4.7 slip event of October 2006 on the Superstition Hills fault, southern California. *Journal of Geophysical Research*, *114*(B7), B07402.

Wei, M., Sandwell, D., Fialko, Y., & Bilham, R. (2011). Slip on faults in the Imperial Valley triggered by the 4 April 2010 Mw 7.2 El Mayor-Cucapah earthquake revealed by InSAR. *Geophysical Research Letters*, *38*(1).